ELSEVIER

Contents lists available at ScienceDirect

Journal of Materials Science & Technology

journal homepage: www.elsevier.com/locate/jmst



Research Article

Strengthening in Al-, Mo- or Ti-doped CoCrFeNi high entropy alloys: A parallel comparison



Xi Li^a, Zhongtao Li^a, Zhenggang Wu^{a,*}, Shijun Zhao^{b,*}, Weidong Zhang^{a,*}, Hongbin Bei^c, Yanfei Gao^d

- ^a College of Materials Science and Engineering & Hunan Province Key Laboratory for Spray Deposition Technology and Application, Hunan University, Changsha 410082, China
- ^b Department of Mechanical Engineering, City University of Hong Kong, Hong Kong, China
- ^cDepartment of Materials Science and Engineering, Center of Electron Microscopy and State Key Laboratory of Silicon Materials, Zhejiang University, Hangzhou 310027, China
- ^d Department of Materials Science and Engineering, University of Tennessee, Knoxville, TN 37996, United States

ARTICLE INFO

Article history: Received 3 January 2021 Revised 17 February 2021 Accepted 28 February 2021 Available online 18 May 2021

Keywords:
CoCrFeNi alloy
Compositional effect
Solid solution strengthening
Grain boundary strengthening
Precipitation strengthening
Stacking fault energy

ABSTRACT

In the current work, a parallel comparison of the influence of Al, Mo and Ti, on the microstructure and strengthening of the CoCrFeNi alloy was conducted. To achieve this, inconsistencies on variables including the extent of alloying, thermomechanical processing and property-evaluation method were avoided. Microstructurally, following cold-rolling, annealing of the 4 at.% Al-doped alloys at 800-1000 °C did not result in phase separation; nevertheless, that of the 4 at.% Mo- and Ti-doped alloys led to the respective formation of σ and η phase and, consequently, caused extra strengthening through the Orowan dislocation bypassing mechanism. Our systematic qualitative analysis and DFT calculations showed that Al and Ti are more effective than Mo in reducing the stacking fault energy (SFE) of the CoCrFeNi alloy, because they can induce more considerable deformation of electronic density, making the gliding of atomic layers easier. Following identical thermomechnical processing, Al-, Mo-, and Ti-doping causes different extent of solid solution strengthening and grain boundary strengthening. Mo causes the most pronounced solid solution strengthening but does not benefit the grain boundary strengthening; in contrast, the effectiveness of grain boundary strengthening is boosted by the doping Al and Ti. Current analyses support that Labusch instead of Fleischer mechanism is applicable to explain the differences in solid solution strengthening, and the observed differences in grain boundary strengthening arise from the different tendency of Al, Mo and Ti to reduce the SFE of CoCrFeNi. In addition, we determined the value of the dimensionless parameter f in the Labusch model for CoCrFeNi-based alloys and observed a close relation between Hall-Petch slope and SFE. Although more in-depth studies are needed to provide full and mechanistic understandings, both these findings in fact presents significant values toward designing novel singlephase high-strength CoCrFeNi-based alloys through manipulating the solid solution and grain boundary strengthening by compositional tuning.

© 2021 Published by Elsevier Ltd on behalf of Chinese Society for Metals.

1. Introduction

With the face centered cubic (fcc) CoCrFeNi alloy [1,2] serving as the starting point for many other high entropy alloys (HEAs) [3,4], alloying effects on CoCrFeNi has been a continuously active topic. Numerous studies were conducted to understand the individual or synergistic effects of alloying elements like Al [5–7], Ti [8–10], Mo [11,12], Nb [13], Zr [14], Cu [15–18], Y [19], and Ta

E-mail addresses: zwu9@hnu.edu.cn (Z. Wu), shijzhao@cityu.edu.hk (S. Zhao), weidongzhang@hnu.edu.cn (W. Zhang).

[20], among many others. Experimental observations showed that the solubility of the alloying elements in the CoCrFeNi alloy varied significantly (e.g., 6–10 at.% for Al, ~5 at.% for Mo, <7 at.% for Ti, <2.5 at.% for Ta and<1 at.% for Y). Alloying different elements beyond their solubility led to the formation of varying new phase(s), such as B2 and bcc phases for Al [5–7], σ and μ phases for Mo [11,12], σ and Laves phases for Ti [8], Laves phase for Ta [20], and CaCu₅-and Ni₃Y-type phases for Y [19]. Consequently, the mechanical properties of the CoCrFeNi-based HEAs were optimizable through appropriate alloying. For example, a fully eutectic microstructure with a mixture of fcc and Co₂Ta-type Laves phases were obtained by alloying 9 at.% Ta to the CoCrFeNi alloy and

^{*} Corresponding authors.

this bulk ultrafine (100–200 nm) lamellar microstructure led to an excellent combination of mechanical properties (1316 MPa yield strength, 2293 MPa fracture strength, and 22.6% plastic strain) [20]. Other representative successes achieved through CoCrFeNi-based alloying include the particle-strengthened CoCrFeNiTi $_{0.2}$ [10] and CoCrFeNiMo $_{\rm X}$ [11] alloys. All of these alloys had their mechanical property data located on the upper-right comer of the strength-ductility "banana diagram", indicating a deviation from the conventionally recognized trade-off that applies to traditional materials.

Mechanical properties of materials, such as strength and toughness, are determined by their microstructure which is in turn directly affected by a few variables include the composition and processing condition/history. Many prior investigations provided much empirical information regarding the compositional effects on the CoCrFeNi alloy; however, a distinct compositional effect is oftentimes not obtainable by comparing these studies due to their lack of consistency in variables other than composition. For example, Wu et al. [1,21], Li et al. [7], Liu et al. [11], Jiang et al. [22], and Shun et al. [9] investigated the microstructure and mechanical behavior of the base CoCrFeNi alloy and the effects of Al, Mo, Ta, and Ti respectively. In their studies, the method to fabricate (e.g., arcmelting or powder metallurgy) the materials and the state (e.g., as-cast state, rolled or recrystallized state) under which the materials were tested were significantly different. In addition to these, the test method applied to evaluate the mechanical properties of the alloys also lack consistency. Thus, the isolation of the compositional effects is hardly achievable due to the co-influence of multiple variables.

Understanding the compositional (type of dopant) effect is essentially important for establishing HEA thermodynamic database and hence building microstructure-based predictive models toward designing advanced alloys with high strength. Toward this understanding, the current work compares the effects of a few representative and most-often-doped "solute" atoms, namely Al, Mo and Ti on the model CoCrFeNi alloy. To meet the goal, inconsistency of variables other than solute type was avoided by making the extent of alloying, fabrication method, and the state under which the alloys were tested identical. Specifically, 4 at.% Al, Mo and Ti were alloyed to the CoCrFeNi alloy to obtain the Co24Cr24Fe24Ni24Al4, $Co_{24}Cr_{24}Fe_{24}Ni_{24}Mo_4$, and $Co_{24}Cr_{24}Fe_{24}Ni_{24}Ti_4$ alloys, respectively. All alloys identically went through arc-melting, drop-casting, homogenization heat treatment, cold-rolling with same thickness reduction and 1-hour recrystallization annealing under the same temperatures. Quasi-static tensile tests were performed on the annealed alloys to assess the mechanical property differences, the origins of which was subsequently identified through comprehensive crystallographic and microstructural characterizations.

2. Experimental and computational methods

Ingots of the base equiatomic CoCrFeNi alloy, and the $Co_{24}Cr_{24}Fe_{24}Ni_{24}Al_4$, $Co_{24}Cr_{24}Fe_{24}Ni_{24}Mo_4$, and $Co_{24}Cr_{24}Fe_{24}Ni_{24}Ti_4$ alloys were fabricated by arc melting the constituent elements (>99.9% pure) in a water-cooled copper hearth under argon atmosphere. To improve chemical homogeneity, the arc-melted buttons were flipped and re-melted five times before drop casting into rectangular cross-section copper molds measuring 12.7 mm \times 25.4 mm \times 127 mm. The drop-cast ingots were homogenized at 1200 °C for 24 hour followed by water quenching. They were then rolled at room temperature along the longitudinal ingot direction to a final thickness of ~1.6 mm (~87% thickness reduction) without cross-rolling or intermediate

annealing. The rolled materials were annealed at 800, 900, 1000, and $1100 \, ^{\circ}$ C for 1 hour, respectively.

Pieces cut from the 1h-annealed rolled sheets were crystal-lographically examined using a Panalytical XPert PRO MRD goniometer equipped with copper radiation (XRD, Cu K α , 40 kV, 40 mA, 1.2°/min) to assess their phase components. The samples were scanned through 2θ ranging from 30 to 90 degrees with a scan rate of 1.2 degree/minute. Microstructures of these materials were characterized using a Quanta 650 FEG SEM operated in the backscattered electron (BSE) mode and a JEOL-2100 TEM high-resolution transmission electron microscope (TEM) coupled with energy dispersive spectrometer (EDS). TEM samples were first ground to ~ 60 μ m and then punched to Φ 3 mm circle sheets, followed by twin-jet electro-polishing using a mixed solution of HNO₃ : CH₄O_{1/4} 1 : 4 under a temperature around 233 K.

The mechanical properties of the alloys were tested using quasi-static tension tests at room temperature. Flat dog-bone-type specimens with a gage length of 9.525 mm cut from the annealed sheets by electrical discharge machining (EDM) with their longitudinal axes perpendicular to the rolling direction were used for the tensile tests. All faces of their gage sections ground through 600-grit SiC paper. Tensile tests were performed with a screw-driven tensile testing machine (SHIMADZU AGS-X 50 KN) with a crosshead speed of 0.572 mm/min (engineering strain rate of 10^{-3} s⁻¹) under room temperature in ordinary ambient air. Full range extensometer (SHIMADZU Non-Contact Digital Video Extensometer) was used for strain measurement. Three nominally identical specimens of each alloy.

First-principles calculations based on density-functional theory as implemented in VASP [23] were performed to shed light on the effects of Al, Ti, and Mo on the SFE of CoCrFeNi alloy. The Perdew-Burke-Ernzerhof (PBE) form of the gradient corrected functional was used to describe the exchange and correlation interactions [24]. Electron-ion interactions were modeled using the projector-augmented-wave PAW method [25]. The energy cutoff for the plane-wave basis set was 400 eV, and the energy convergence was 10^{-6} eV. Spin-polarization was considered in all calculations. The axial interaction model (AIM) [26,27] was adopted to calculate averaged SFEs for alloys with different compositions based on the constructed special quasirandom structures (SQS) with optimized short-range order parameters [28,29] through a simulated annealing algorithm [30]. Specifically, SQS supercells containing 144 atoms were prepared to calculate the energies required to calculated SFE. Three structures were considered namely, fcc, hcp, and dhcp structures. The SFE was then calculated by $\gamma_{\rm ISF} =$ $\frac{(E_{\rm hcp}+2E_{\rm dhcp}-3E_{\rm fcc})}{A}$, where $E_{\rm dhcp}$, $E_{\rm hcp}$, and $E_{\rm fcc}$ are the total energy per atom of the dhcp, hcp and fcc phase, respectively, and A is the stacking fault area. Both the cell parameters and internal coordinates were fully optimized and three independent SQS supercells were calculated and the energies were averaged to calculate SFE. We have checked the convergene of the average energy from the three SQS supercell. For example, for CoCrFeNi+Al, the standard deviation of the energy of the three FCC SQS supercells is only 3 meV/atom.

Although the SFEs from the AIM model represent average values of the considered alloys, it is difficult to understand the observed trend. Therefore, we also employed the slab model to probe the changes near the stacking fault region induced by Al/Mo/Ti dopants [30,31]. With the slab model, the SFEs would depend on the distribution of the alloying elements. Therefore, we carried out selective calculations to reveal the different effects of Al/Mo/Ti dopants. The charge density derived from the slab model was used to analyze the alloying effects from different dopants.

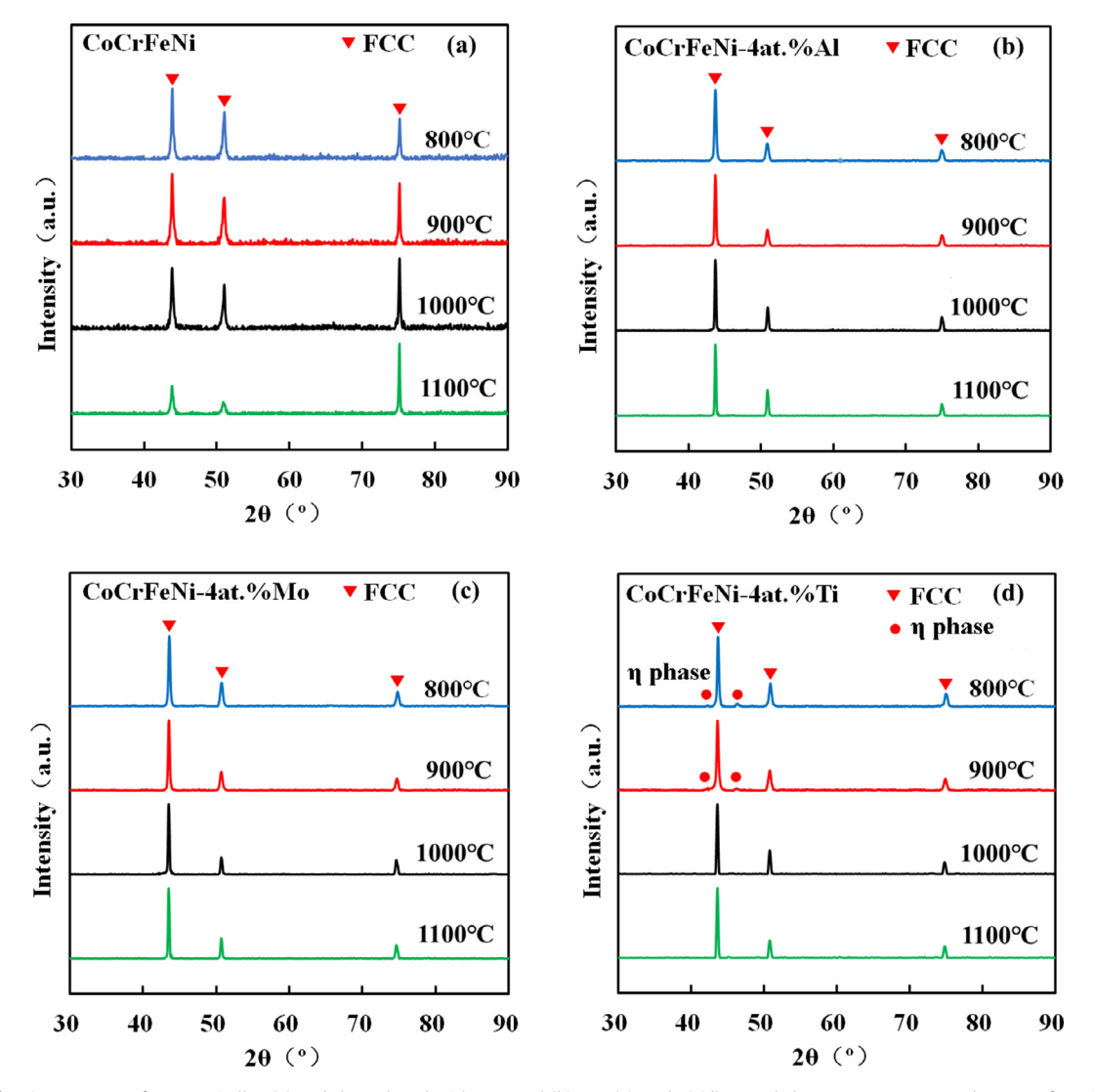


Fig. 1. X-ray diffraction patterns of CoCrFeNi alloy (a) and those doped with 4 at.% Al (b), Mo (c), and Ti (d) annealed at 800, 900, 1000 and 1100 °C for 1 h following room temperature rolling.

3. Results and discussion

3.1. Phase components and microstructure

Fig. 1 shows the XRD patterns for the investigated alloys annealed at different temperatures following cold rolling. For CoCrFeNi, Co₂₄Cr₂₄Fe₂₄Ni₂₄Al₄ and Co₂₄Cr₂₄Fe₂₄Ni₂₄Mo₄ alloys annealed at all temperatures, only diffraction peaks corresponding to fcc phase were observed. Additional peaks existed for the 800 °C- and 900 °C-annealed Co24Cr24Fe24Ni24Ti4 alloys, indicating the presence of secondary phase(s). The corresponding BSE images were presented in Fig. 2. The presence of only fcc phases in the CoCrFeNi alloy and that doped with Al at all annealing temperatures was confirmed. For the Co24Cr24Fe24Ni24Mo4 alloy, a large number of particles with bright contrast were observed in the 800 °C-annealed specimen; these particles located mainly along the grain boundaries; the volume fraction of the particle was significantly reduced when the annealing temperature increased to 900 °C; annealing at higher temperatures (1000 and 1100 °C) did not result in the formation of secondary-phase particles. Secondaryphase particles were also observed in the 800 °C- and 900 °Cannealed 4 at.% Ti-doped alloys; they exhibit lighter contrast and are nearly morphologically parallel with each other (Fig. 2).

We performed further microstructural characterizations using TEM to identify the nature of the precipitates; the obtained TEM micrographs for the 800 °C-annealed specimens were presented in Fig. 3 in which that of the 800 °C-annealed $Co_{24}Cr_{24}Fe_{24}Ni_{24}Al_4$ alloy (Fig. 3(a)) was also included to confirm its single phase nature. Compositional analysis on the near-spherical precipitates (Fig. 3(b)) for the $Co_{24}Cr_{24}Fe_{24}Ni_{24}Mo_4$ alloy showed their richness in Mo and Cr. The diffraction spot of representative precipitates indicated that they possess a tetragonal structure. Faint streaks appear in the SAED pattern, hinting that SFs exist in this region. These information indicates that the main precipitates in the $Co_{24}Cr_{24}Fe_{24}Ni_{24}Mo_4$ alloy was sigma phase (σ phase). In fact, the precipitation of sigma phase in Mo-containing CoCrFeNi alloys have been reported previously by a number of researchers [11,12].

The platelet precipitates with a hcp structure observed in Fig. 3(c) are rich in Ti with a composition close to (Ni, Co)₃Ti. From the SAED and HRTEM images, we can see that the platelet precipitates in the $Co_{24}Cr_{24}Fe_{24}Ni_{24}Ti_{4}$ alloy grew and elongated in a specific direction ($\langle 1\bar{1}00\rangle$) with a narrow thickness and thickened in step-by-step in $\langle 0001\rangle$ direction. The formation of secondary platelet precipitates was also observed in Fig. 3(d). The misorientation between the first and secondary one was ~ 70° around $<11\bar{2}0>$ axis. The lattice spacing of (0001) was measured to be

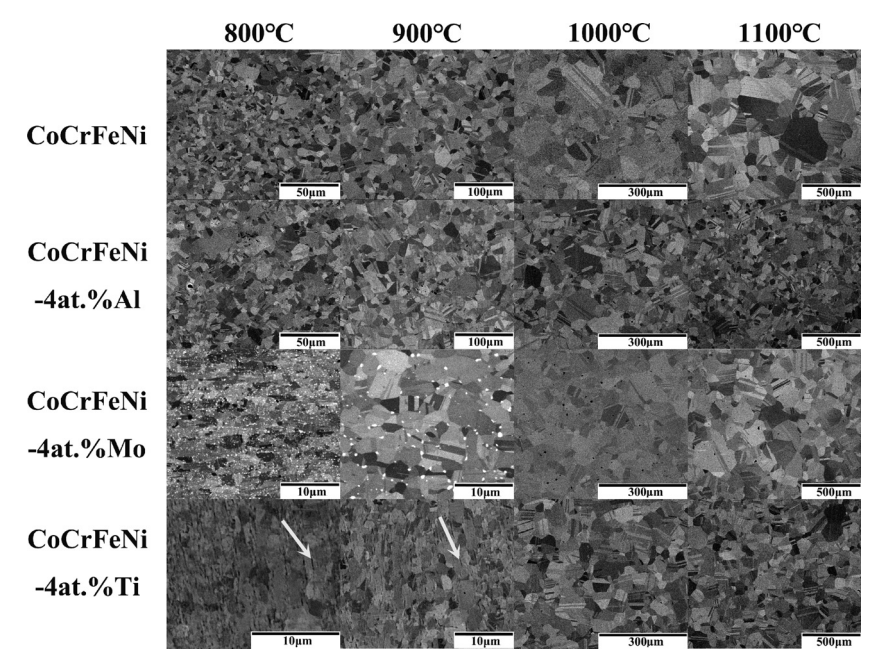
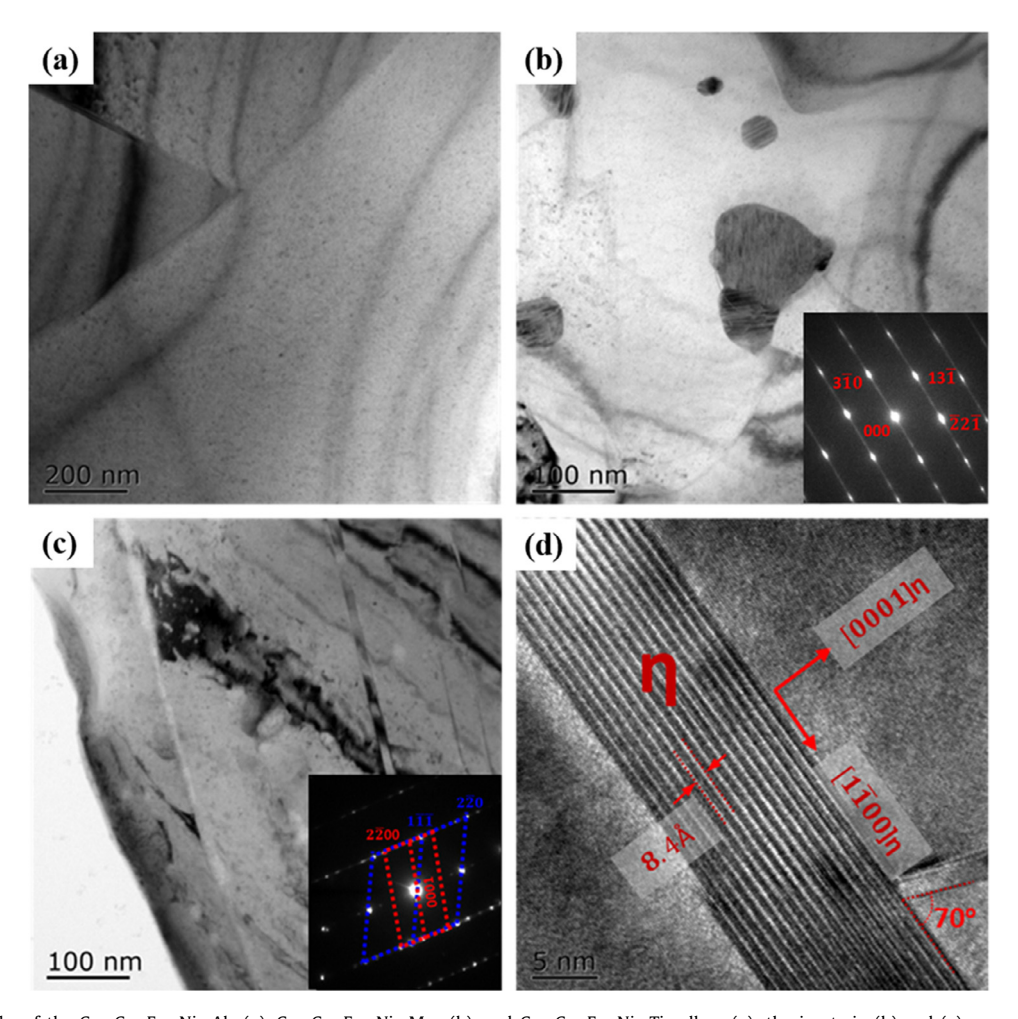


Fig. 2. Back-scattered electron image of CoCrFeNi alloy (a) and those doped with 4 at.% Al (b), Mo (c), and Ti (d) annealed at 800, 900, 1000 and 1100 °C for 1 h following room temperature rolling.



 $\textbf{Fig. 3.} \ \ \text{TEM micrographs of the } \ Co_{24}Cr_{24}Fe_{24}Ni_{24}Al_4 \ \ (a), \ Co_{24}Cr_{24}Fe_{24}Ni_{24}Mo_4 \ \ (b), \ \text{and} \ \ Co_{24}Cr_{24}Fe_{24}Ni_{24}Ti_4 \ \ \text{alloys} \ \ (c); \ \text{the insets in} \ \ (b) \ \ \text{and} \ \ \ (c) \ \ \text{present the SAED patterns of the corresponding observable particles;} \ \ (d) \ \ \text{HRTEM image of the particle present in the } \ \ Co_{24}Cr_{24}Fe_{24}Ni_{24}Ti_4 \ \ \text{alloys}.$

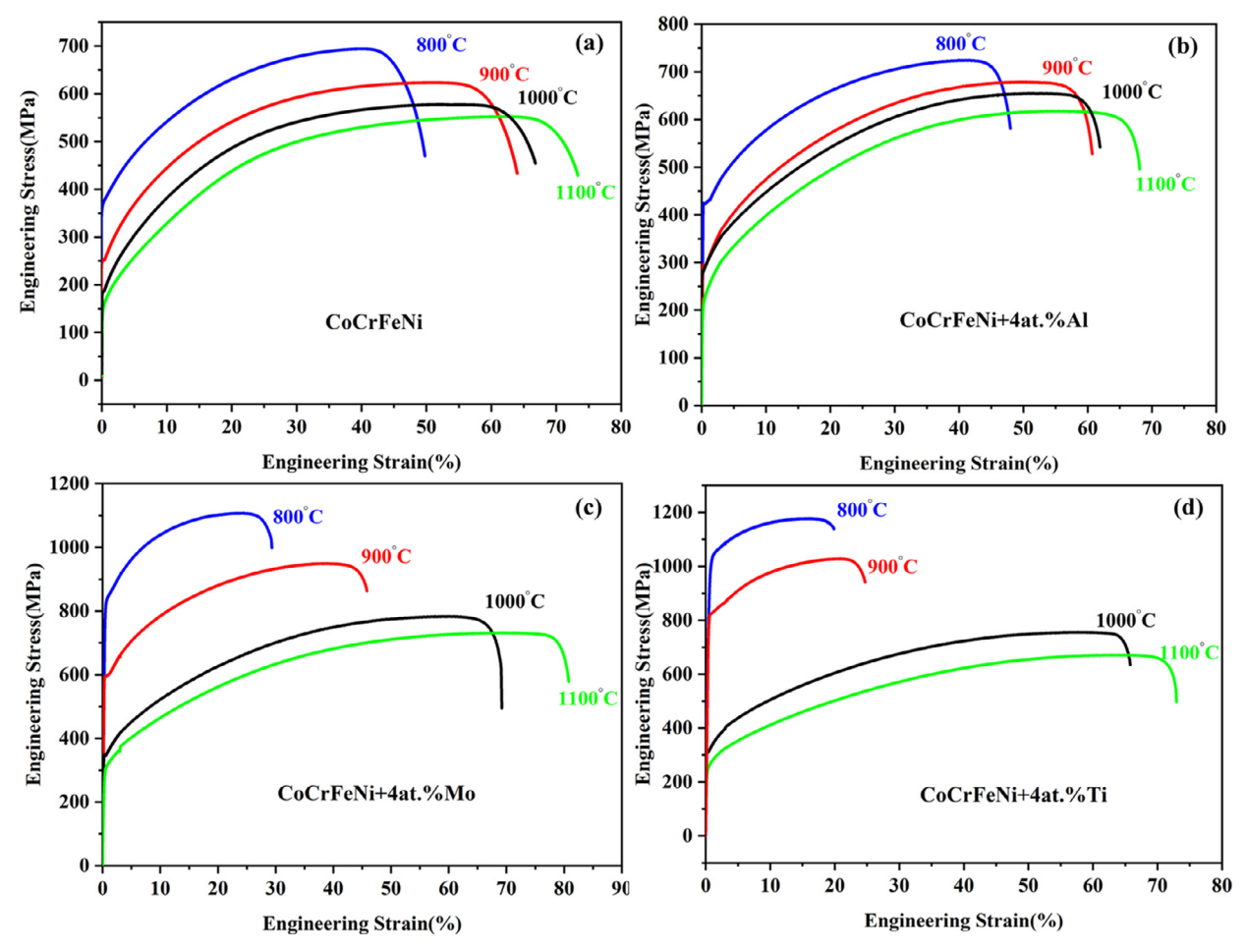


Fig. 4. Representative engineering stress-strain curves of the CoCrFeNi alloy (a) and those doped with 4 at.% Al (b), Mo (c), and Ti (d) annealed at 800, 900, 1000 and 1100 °C for 1 h following room temperature rolling.

~ 8.4 Å (Fig. 3(d)). [110] $_{\gamma}$ /[1120] $_{\rm precipitate}$ was established. All of the obtainable information suggested that the platelet precipitates in the Co $_{\rm 24}$ Cr $_{\rm 24}$ Fe $_{\rm 24}$ Ni $_{\rm 24}$ Ti $_{\rm 4}$ alloy are the Ni $_{\rm 3}$ Ti-type η phase which was frequently seen in Ti-containing Ni–Co-based (super)alloys [32–35].

3.2. Mechanical properties

Representative engineering stress-strain curves of the annealed alloys were presented in Fig. 4. For all 4 alloys, the stress-strain curves shifted up as annealing temperature decreases from 1100 to 800 °C, accompanied with a monotonic ductility decrease. In terms of yield strength (σ_V), the 4 at.%-doping caused strengthening to the CoCrFeNi base alloy, the extent of which varies with "solute" atoms. After annealing at all temperatures, the strengthening effects from Mo- and Ti-doping were more pronounced than that from Al-doping. For example, after 1 hour annealing at 800 °C, the CoCrFeNi "solvent" alloy had a yield strength of ~ 375 MPa and the values of the 4% Al-, Mo-, and Ti-doped alloys reached ~ 425, 830, and 1030 MPa, respectively. Another finding was that the relative strengthening effects from Mo, and Ti-doping changes as annealing temperature. Upon annealing at 800 and 900 °C, 4% Ti-doping displayed much more pronounced strengthening than Mo-doping; and reverse trend was observed when the anneals were conducted at 1000 and 1100 °C.

The yield strength of the annealed specimens for each alloy extrapolated from the engineering stress-strain curves were presented in Fig. 5 as a function of grain size (*d*) calculated from the

corresponding BSE images (Fig. 2) using the interception method. Data points for single-phase materials were presented as closed circles and those precipitate-existing alloys as open circles. It can be seen that a good fit to $\sigma_Y \propto \frac{1}{\sqrt{d}}$ can be made for the CoCrFeNi and Al-doped CoCrFeNi alloy. This classic Hall-Petch relationship [36,37] is well recognized applicable to single phase polycrystalline metals with d in the micro-meter range, given by

$$\sigma_{\rm Y} = \sigma_{\rm i} + k_{\rm HP} d^{-\frac{1}{2}} \tag{1}$$

where σ_i is the intrinsic strengthening, and $k_{\rm HP}$ is the Hall-Petch coefficient representing the degree of grain boundary strengthening.

In order to reveal the full Hall-Petch relation for the single phase Co₂₄Cr₂₄Fe₂₄Ni₂₄Mo₄ and Co₂₄Cr₂₄Fe₂₄Ni₂₄Ti₄ alloys, additional annealing steps were conducted at temperatures in their single-phase range (1050 and 1150 °C) and tensile-tested the obtained specimens. The data points were added to Fig. 5 as closed squares. Table 1 lists the fitted values of σ_i and k_{HP} . These values for the CoCrFeNi alloy are consistent with that derived from previous study [21]. The solid solution strengthening (σ_{ss}) caused by 4 at.% Al-, Mo- and Ti-doping were calculated using the difference in σ_i between the doped alloys and the CoCrFeNi "solvent" alloy. The so-obtained σ_{ss} values (Table 1) for 4 at.% Al-, Mo- and Ti-doped alloys were ~ 35.6, 143.8 and 82.5 MPa, respectively. For the 800 °C- and 900 °C-annealed $Co_{24}Cr_{24}Fe_{24}Ni_{24}Mo_4$ and Co24Cr24Fe24Ni24Ti4 alloys, their extra strengthening resulted from the corresponding secondary phases particles were calculated as the differences (i.e., $\sigma_{Y}-\sigma_{Y,HP}$ in Table 1) between the

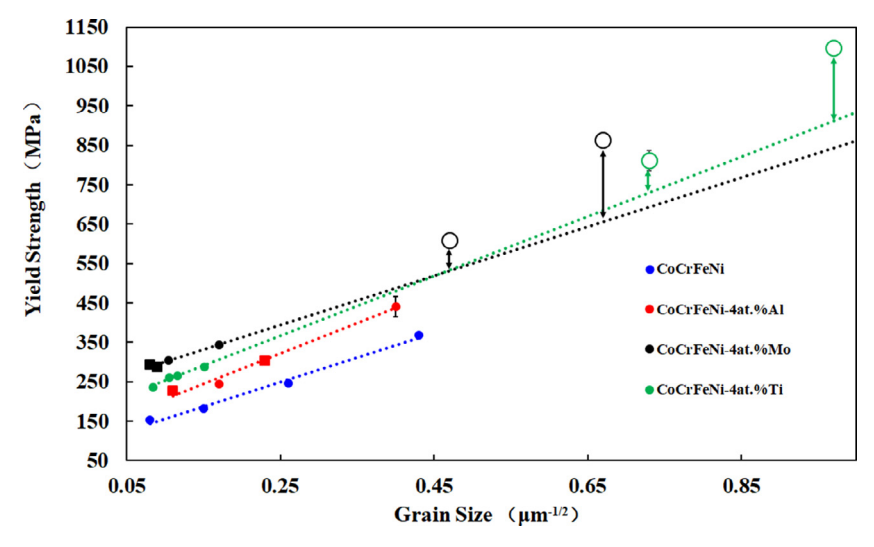


Fig. 5. Hall-Petch plots showing the effects of grain size, d, on the yield strength, $σ_Y$, for the CoCrFeNi alloy and those doped with 4 at.% Al, Mo and Ti; the black and green open circles respectively indicate the 800 °C- and 900 °C-annealed $Co_{24}Cr_{24}Fe_{24}Ni_{24}Mo_4$ and $Co_{24}Cr_{24}Fe_{24}Ni_{24}Ti_4$ alloys; the closed squares correspond to those with additional annealing.

Table 1 Curve fitting values (σ_i and k_{HP} in Eq. (1)), solid solution strengthening (σ_{ss}) and precipitation strengthening (σ_{ppt}) effects of the studied alloys.

	$\sigma_{\rm i}$ (MPa)	$k_{\mathrm{HP}}~(\mathrm{MPa}{\cdot}\mu\mathrm{m}^{-1/2})$	$\sigma_{ m ss}$ (MPa)	$\sigma_{ m ppt}$ (800 °C, MPa)		σ _{ppt} (900 °C, MPa)	
				σ_{y} - σ_{y-HP}	$\sigma_{ m Orowan}$	σ_{y} - σ_{y-HP}	$\sigma_{ m Orowan}$
CoCrFeNi	94.9	621.1	0	-	-	_	-
CoCrFeNi-4%Al	130.5	765.8	35.6	-	-		-
CoCrFeNi-4%Mo CoCrFeNi-4%Ti	238.7 177.4	623.6 756.4	143.8 82.5	171.5 185.5	221 154.5	72.5 82	51.6 85.2

experimentally-measured σ_Y and the expected one through the Hall-Petch relation $(\sigma_{Y,HP})$ as indicated by the double arrows in Fig. 5. It can be seen that for both alloys, annealing at lower temperatures resulted in more pronounced precipitate strengthening. Another phenomenon that can be derived from Table 1 is that the Hall-Petch coefficient of the CoCrFeNi alloy did not change much by 4 at.% Mo doping; nevertheless, Al- and Ti-doping boosted the coefficient by ~ 23%. In the next sections, we performed systematic quantitative and qualitative investigations and analysis to understand the underlying strengthening mechanisms of this series of alloys.

In the next sections, we performed systematic quantitative and qualitative investigations and analysis to understand the underlying mechanistic origins to the observed differences on the effects of Al, Mo, and Ti on the solid solution strengthening (σ_{ss}), grain boundary strengthening effectiveness (k_{HP}), and secondary phases ($\sigma_{Y} - \sigma_{Y,HP}$) strengthening of the model CoCrFeNi alloy.

3.2.1. Solid solution strengthening

Conventional solid solution theories were developed by assuming that dislocations move through a solvent lattice and encounter discrete solutes atoms that affect their mobility. A general case to consider is the energetics of, and the force resulting from, the elastic interaction of a dislocation with the strain field of a single solute atom [38–44]. Two most important contributors to this interaction include the atomic size (a) misfit ($\varepsilon_a = \frac{1}{a} \frac{da}{dc}$) and modulus (G) mismatch ($\varepsilon_G = \frac{1}{G} \frac{dG}{dc}$) between the solute and solvent atoms. Fleischer considered separations between strong obstacles and so developed a relationship of $\sigma_{\rm ss} \propto c^{\frac{1}{2}}$, where c is the solute molar concentration [45–49]. A relationship of $\sigma_{\rm ss} \propto c^{\frac{2}{3}}$ was developed by Labusch through a statistical treatment of a dislocation moving through an array of obstacles with a distribution of interaction

strengths [50-52]. The expressions for these two descriptions are:

Fleischer:
$$\sigma_{ss} = \frac{MG\varepsilon_{\rm f}}{700}c^{\frac{1}{2}}$$
 (2)

Labusch:
$$\sigma_{ss} = fG\varepsilon_1 c^{\frac{2}{3}}$$
 (3)

where $\varepsilon_f = |\frac{\varepsilon_G}{1+0.5|\varepsilon_G|} - 3\varepsilon_a|^{\frac{3}{2}}$ and $\varepsilon_l = [(\frac{\varepsilon_G}{1+0.5|\varepsilon_G|})^2 + \alpha^2\varepsilon_a^2]^{\frac{2}{3}}$ represent the overall contributions from elastic misfit, M=3.06, f is a dimensionless fitting parameter, and α is a dimensionless parameter that describes the type of dislocations (for example, $\alpha \le 16$ for screw dislocations and $\alpha \ge 16$ for edge dislocations). In this present study, $\alpha=16$ was used. It is widely accepted that the Fleischer model is applicable at dilute concentrations and the Labusch model works in the concentration regime [53-55]. Leyson and Curtin [56] suggested that in conventional alloys, the critical concentration beyond which the strengthening mechanism switches could be as low as 10^{-4} . For multi-component equi- or nearequiatomic alloys, although they were normally treated as mythical pure "average solvents" since there is no "solvent" or "solute" in the conventional sense, their solid solution strengthening effects were very often found explainable and predictable using the Labusch model [57–59]. When these HEA "solvents" were alloyed in the conventional manner, there is so far no consensus on the applicable strengthening mechanism (Fleischer or Labusch). Tong et al. [10] and Wang et al. [60] used the Fleischer model to calculate σ_{ss} for the 4.7 at.% Ti-doped CoCrFeNi and 3.1 at.% Modoped CoCrNi alloys, respectively. Varvenne and Curtin [61] extended the Labusch-type model to successfully predict the solid solution strengthening of Al-doped CoCrFeNi and CoCrFeNiMn alloys with simplifications such as rule-of-mixture elastic constant and atomic volume. The following analysis was conducted to un-

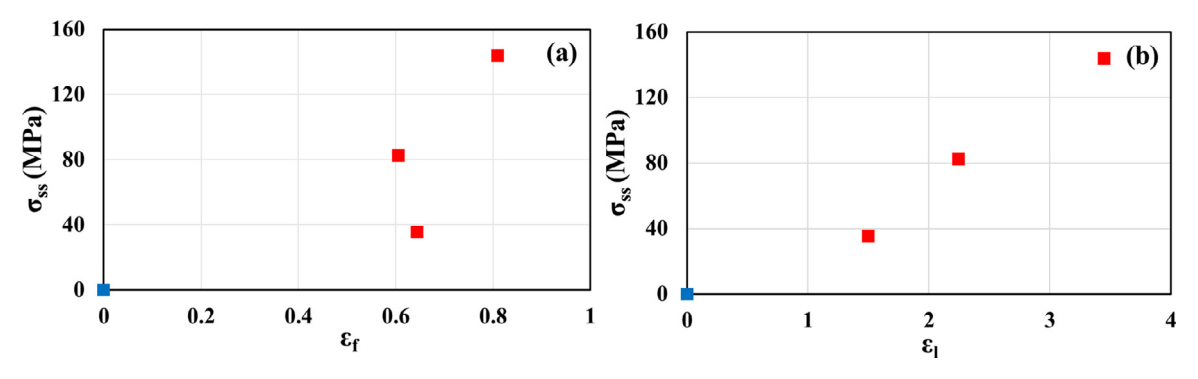


Fig. 6. Relationships of (a) $\sigma_{ss} \sim \varepsilon_f$ and (b) $\sigma_{ss} \sim \varepsilon_l$, in which σ_{ss} values are cited from Table 1. ε_f and ε_l represent the overall contributions from elastic misfit and were calculated using the atomic size misfit (ε_a) and modulus mismatch (ε_G).

derstand the underlying solid solution strengthening mechanism for the 4 at.% doped CoCrFeNi-series alloys.

To achieve the above-mentioned goal, ε_a and ε_G were calculated by assuming a linear a-c and G-c relation within 0-4 at.% range. The lattice constants (a, 3.5715, 3.5827, 3.5938, 3.5876 Å for CoCrFeNi, Co₂₄Cr₂₄Fe₂₄Ni₂₄Al₄, Co₂₄Cr₂₄Fe₂₄Ni₂₄Mo₄, and Co₂₄Cr₂₄Fe₂₄Ni₂₄Ti₄ alloys respectively) for this calculation were determined from the XRD patterns. Shear modulus (G) for the calculation were determined using the rule-of-mixture method as suggested by Varvenne and Curtin [61] in cases of dilute doping. According to Eqs. (2) and (3), when the CoCrFeNi "solvent" was doped with the same concentration but different type of solutes, differences in elastic misfit (ε_f and ε_1) could cause varying extent of solid solution strengthening and a linear relationship of $\sigma_{ss} \sim \varepsilon_{f}$ or $\sigma_{\rm ss} \sim \varepsilon_{\rm l}$ should be expected. The $\sigma_{\rm ss}$ values (Table 1) were plotted as a function of ε_f and ε_l values in Fig. 6. It can be clearly seen that the correlation between σ_{ss} and ε_f significantly deviates from linearity (Fig. 6(a)). In contrast, a good linear relationship between σ_{ss} and ε_1 except for the origin (0, 0) was achieved (Fig. 6(a)), indicating that the Labusch model can be used to explain the solid solution strengthening in the CoCrFeNi-based alloys with ~ 4 at.% doping. The linear expression can be expressed as: $\sigma_{ss} = -50 + 55.6\varepsilon_l$, in the unit of MPa. The failure of the linear relation to pass through the (0, 0) origin and the negative intercept indicate the existence of a critical doping concentration below which another model (e.g., Fleischer model) could be used. However, the identification of this critical point is not attainable in the current study. It is noted that the slope of the linear relation is $fGc^{\frac{2}{3}}$, where c = 0.04 and G = 84 GPa [21] in this study. Therefore, for CoCrFeNi-based dilute alloys, taking the effects of solute concentration into account, the amount of solid solution strengthening could be derived as

$$\sigma_{ss} = -50 + 475.5\varepsilon_1 c^{\frac{2}{3}} \tag{4}$$

Firstly, assuming for certain type of solute, the Hall-Petch coefficient varies linearly with the doping concentration. Secondly, the dimensionless parameter f remains as a constant for all CoCrFeNi-based dilute alloys as treated elsewhere [56]. Therefore, using the dimensionless parameter f obtained from the linear relation in Fig. 6(b), we are able to respectively calculate the grain boundary strengthening and solid solution strengthening effects in a few previously reported doped (2.44–6.98 at.%) single phase CoCrFeNi alloys. Eventually, adding up the intrinsic strength (94.9 MPa) of the base CoCrFeNi alloy, the predicted yield strengths ($\sigma_{\rm predicted}$) matched nicely with the experimentally measured values ($\sigma_{\rm experiment}$), as shown in Fig. 7.

The above analysis suggests that the solid solution strengthening in the "dilute" doped CoCrFeNi alloys could be dominated by the Labusch strengthening mechanism in which, with the ap-

plied shear stress, the gliding non-straight dislocation line will constantly morph its shape and thus requires additional stress to move in the forest of "stress centers" [57]. Moreover, the quantification of the dimensionless parameter f and its proved applicability to quantitatively predict the solid solution strengthening effects in CoCrFeNi-series alloys [11,21,62–65] with a much broader range of concentration (\sim 2–7 at.%) present significant values for designing more single-phase high-strength CoCrFeNi-based alloys.

3.2.2. Grain boundary strengthening

The effectiveness of the grain boundary strengthening is usually manifested through the Hall-Petch coefficient ($k_{\rm HP}$) [36,37]. It was previously mentioned that, compared to the CoCrFeNi "solvent" alloy, doping 4 at.% Mo did not result in significant change in the value of $k_{\rm HP}$ which was moderately enhanced by 4 at.% Al- and Ti-doping. The direct and precise causes for the observed $k_{\rm HP}$ differences are not obtainable in the current study; instead, a qualitative analysis was provided to propose possibilities as follows. A relatively more-widely accepted mechanistic interpretation of the grain boundary strengthening is on the basis of the presence of geometrically necessary dislocations (GNDs) resulting from the additional local deformation gradients that are needed to maintain compatibility among grains [66-68]. GNDs density would be closely affected by the easiness of the dislocations to cross-slip which will cause the reduction of it. One important materialsrelated intrinsic property that exerts significant influence on dislocation cross-slip is the stacking fault energy (SFE) through its determination on the easiness of unit dislocations to dissociate into partial dislocations [66–71]. Low value of SFE normally promotes dislocation dissociation and thus hinders dislocation cross-slip. The formation of annealing twins is also promoted by the low SFE. Annealing twins can act as dislocation movement barrier and hence as additional strengtheners, the effectiveness of which could be reflected in and integrated into $k_{\rm HP}$. Thus, a larger grain boundary strengthening effect manifested by a higher value of k_{HP} is reasonably expected for metals with lower SFE. The following qualitative and quantitative analyses were performed to explore the relative efficiency of Al-, Mo- and Ti-doping on SFE of CoCrFeNi.

Qualitatively, using the probabilities of occurrence of such defects as stacking faults and twins, He et al. [72] suggested that adding Al and Ti to the CoCrFeNi HEA decreased its value of SFE. Using X-ray line profile method, Cai et al. [73] estimated the SFE of the as-extruded 2.3 at.% Mo-doped CoCrFeNi alloy to be 19 mJ/m², which is lower than that reported for or the CoCrFeNi alloy (~ 32 mJ/m²). In contrast, He et al. [72] suggests an increase of SFE by Mo-doping. Based on calculation using density functional theory, Yu et al. [74] also found that Al is a more efficient SFE-reducer than Mo to the CoCrFeNi alloy. Wen et al. [75] found that the atomic radius difference (Δ R) as well as valence electron count difference (Δ VEC) between solute atoms and solvent atoms have

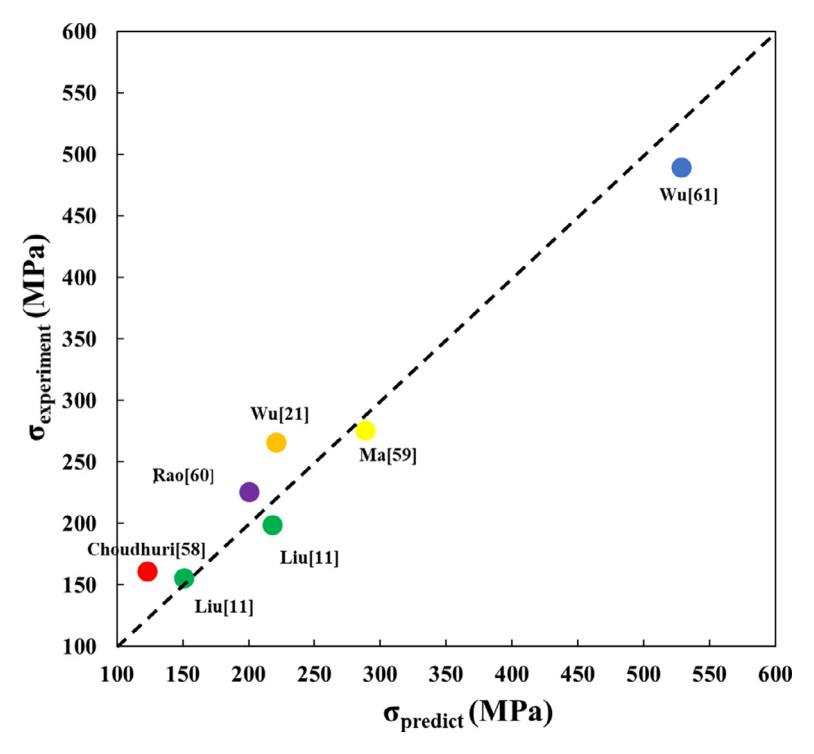


Fig. 7. Predicted vs. experimental yield strength due to "dilute" doping of the CoCrFeNi alloy; the prediction was made using Eq. (1) by applying the dimensionless parameter f obtained from the linear relation in Fig. 5b to Eq. (3) and assuming a linear relation between k_{HP} and doping concentration;

Table 2 Atomic radii and valence electron count (VEC) for each element [76–78].

	Со	Cr	Fe	Ni	Al	Мо	Ti
Atomic radius (Å)	1.251	1.249	1.241	1.246	1.432	1.363	1.462
VEC	9	6	8	10	3	6	4

influence on the SFE in fcc alloys, with larger ΔR and ΔVEC tend to drag down the SFE. Following this, in order to perform a qualitative analysis on their relative effects on the SFE the CoCrFeNi alloy, we first treat the CoCrFeNi alloy as an "average pure solvent" and then estimate the atomic radii and VECs of this series of alloys using the rule-of-mixture based on the corresponding values of each single element [76–78] (Table 2). The calculated atomic radii for CoCrFeNi, $Co_{24}Cr_{24}Fe_{24}Ni_{24}Al_4$, $Co_{24}Cr_{24}Fe_{24}Ni_{24}Mo_4$, and $Co_{24}Cr_{24}Fe_{24}Ni_{24}Ti_4$ alloys are 1.2467, 1.2542, 1.2514, 1.2554 Å, respectively; and the VEC counts are 8.25, 8.04, 8.16, 8.08 respectively. It is obvious that ΔR and ΔVEC resulted from the Al and Ti doping are comparable and significantly larger than that from Modoping, indicating the stronger tendency of Al and Ti to reduce the SFE.

Quantitatively, we have calculated SFEs of the pristine CoCrFeNi alloy and Al/Ti/Mo doped CoCrFeNi alloys based on first-principles calculations. With the AIM model, our results yield a SFE value of $-13.5 \, \text{mJ/m}^2$ for pristine CoCrFeNi at 0 K. The negative SFE has also been found in previous theoretical calculations [30], an indication of low SFE for this HEA at low temperatures. The AIM model is further used to evaluate the influence of Al/Ti/Mo doping on SFEs of CoCrFeNi. The obtained results are -25.1, -24.0, and $-13.0 \, \text{mJ/m}^2$ for Al-doped, Ti-doped, and Mo-doped CoCrFeNi, respectively. As SFE characterizes the energy difference between FCC and HCP structures, a negative SFE would imply that HCP phase would prefer in the considered alloy, at least locally at low temperatures. Such negative SFEs have been found in a number of HEAs, corresponding to their excellent mechanical properties by enabling deformation twinning. In this study, the minor dopants

of Al/Mo/Ti slightly change the SFE values of CoCrFeNi, thus affecting its strengthening mechanism.Doping with Al and Ti has similar effects on SFEs, both decreasing the SFE of CoCrFeNi. On the other hand, Mo doping leads to a insignificant change of SFEs. These results are in line with the qualitative analysis as discussed above.

The AIM model represents averaged SFE values since different SQS supercells are used to calculate the energies for fcc, hcp, and dhcp structures. As a result, elemental specific information is difficult to obtain for this method. To gain insight into the different roles of these three dopant elements, we have employed the supercell model to explicitly include the SFE in the calculations. After relaxation, we compare the spin density plot in one of the [110] planes in Fig. 8. For fcc alloys, it is suggested that the spin charge density is suitable to analyze elasticity-related properties [79]. It can be seen that these three elements all have small spin density, which leaves an empty region. Nevertheless, these dopant elements induce different degrees of deformation in the spin density of nearby elements. Specifically, both Al and Ti lead to asymmetric deformation of nearby spin density distributions, whereas the influence of Mo is symmetric. The asymmetric change of spin density due to Al/Ti may accommodate the shear deformation easily due to the ease of charge redistribution, resulting in the low SFEs. On the other hand, Mo doping imposes small perturbation of the charge density distribution, leading to similar SFEs as the pristine

A combination of our qualitative analysis and quantitative calculation provided appropriate evidences that doping Al and Ti to the CoCrFeNi alloy is more efficient than doping Mo in reducing its SFE, given that the critical concentration beyond which phase

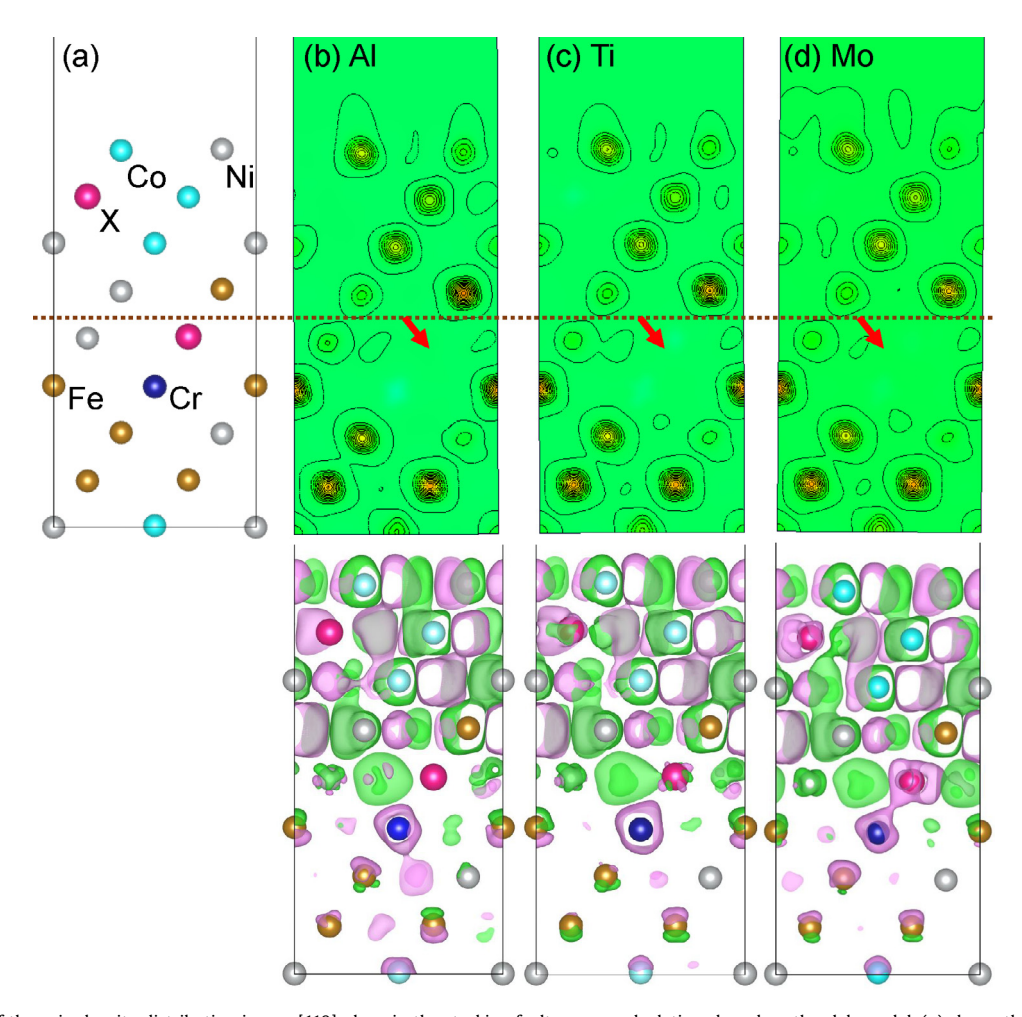


Fig. 8. Comparisons of the spin density distribution in one [110] plane in the stacking fault energy calculations based on the slab model. (a) shows the computational model, in which the red atom denotes the dopant element X, (b)-(d) shows the spin density distribution for Al, Ti, and Mo, respectively. The location of the dopants is indicated by the red arrow. The lower panels shows the spin density difference before and after the introduction of stacking fault. Charge accumulation is represented by red while depletion by green. An isovalue of 0.004 e/Å3 was used.

separation would occur not reached. This was further supported by our measurement of the annealing twin density (ρ_{twin} , which, in fcc metals, exhibits well-recognized inverse relation with the SFE [80-82]) on the investigated alloys (Fig. 9), showing that compared to ho_{twin} of the CoCrFeNi alloy, that of the Mo-doped alloy was comparable and that of both Al- and Ti-doped alloys were reduced by 26%-32%. It is readily to see that relative differences of K_{HP} values of the doped alloys compared to the CoCrFeNi alloy followed well the expected trend of the SFE-reduction efficiency, indicating a close relation between $K_{\rm HP}$ and SFE. In fact, similar observations were reported before by a few although limited number of researchers, such as Astafurov et al. [83] and Wang and Murr [84]. However, none of these previous studies have provided suitable mechanistic explanation behind of experimental phenomena. Our current reasoning indicates that the variation of SFE with doping element could be one of the important causes for the observed differences in the grain boundary strengthening effect through the effects of SFE on dislocation cross-slip and thus the GNDs density and/or the annealing twin density. Mechanics models are under development to provide further understanding on the SFE- K_{HP} close relation.

3.2.3. Particle strengthening

For the 800 °C- and 900 °C-annealed $Co_{24}Cr_{24}Fe_{24}Ni_{24}Mo_4$ and $Co_{24}Cr_{24}Fe_{24}Ni_{24}Ti_4$ alloys, secondary-phase particles (i.e. the near-spherical and platelet precipitates) also contributed to their

strength. Based on the nature (structure and morphology) of the σ phase in the $\text{Co}_{24}\text{Cr}_{24}\text{Fe}_{24}\text{Ni}_{24}\text{Mo}_4$ alloy and η phase in the $\text{Co}_{24}\text{Cr}_{24}\text{Fe}_{24}\text{Ni}_{24}\text{Ti}_4$ alloy, their strengthening to the fcc matrix is most likely through the well-known Orowan mechanism in which extra stresses are needed for dislocations to bypass the hard precipitates after which the density of dislocations increases by generating fresh dislocation loops. For polycrystalline materials, the increment in yield strength result from Orowan strengthening can be estimated using the Orowan-Ashby equation [85]:

$$\sigma_{\text{Orowan}} = \frac{0.13Gb}{\lambda} \ln \frac{D}{2b} \tag{5}$$

where G=84 GPa is the matrix shear modulus, b=0.251 nm is the Burgers vector, D is the average particle diameter, $\lambda=D[(\frac{1}{2V_p})^{\frac{1}{3}}-1]$ is the interparticle spacing (V_p is the volume fraction of the precipitates). For the calculation of the strengthening from Eq. (3), we measured the volume fraction of the σ phase (\sim 11% and 4% for 800 °C- and 900 °C-annealed specimens) and η phase (\sim 13% and 6% for 800 °C- and 900 °C-annealed specimens) for the 800 °C- and 900 °C-annealed specimens based on their BSE images and/or STEM micrographs. For the σ phase in the Co₂₄Cr₂₄Fe₂₄Ni₂₄Mo₄ alloy, we were also able to calculate the D values from the corresponding micrographs (\sim 100 and 250 nm for 800 °C- and 900 °C-annealed specimens). However, for the Co₂₄Cr₂₄Fe₂₄Ni₂₄Ti₄ alloys, since the η phase had a platelet instead of spherical or near-spherical morphology, direct measurement of

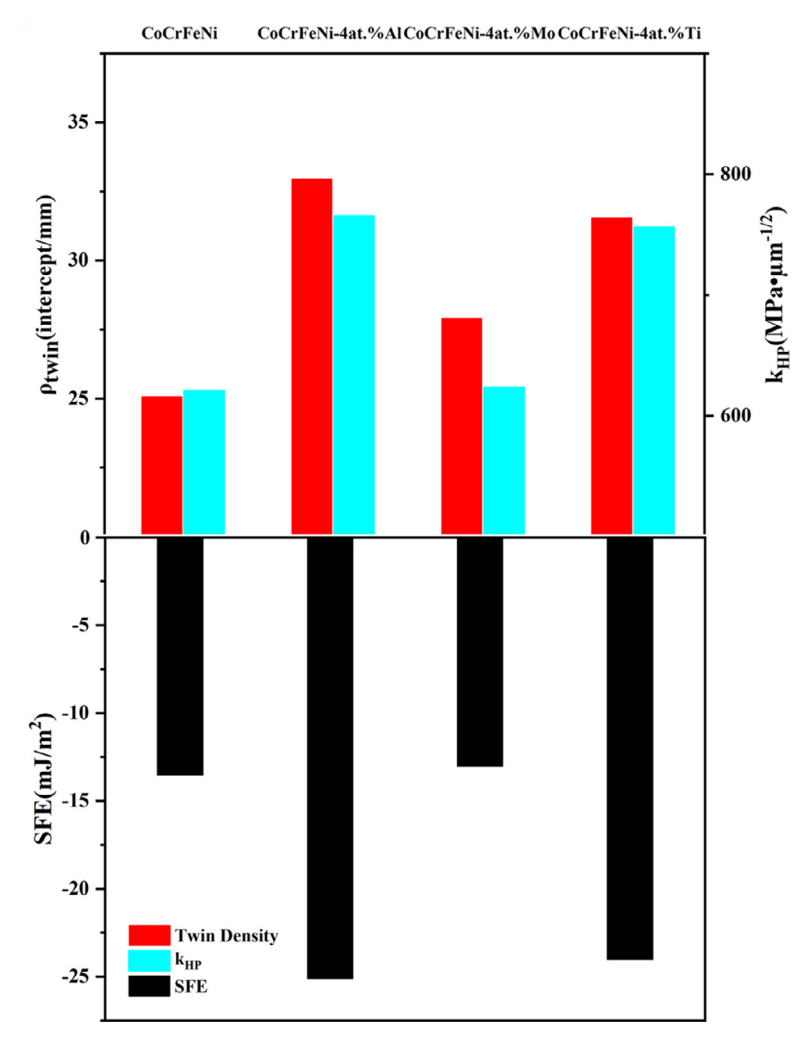


Fig. 9. Stacking fauly energies (SFEs), annealing twin densities ($ρ_{twin}$) and k_{HP} values of the CoCrFeNi, $Co_{24}Cr_{24}Fe_{24}Ni_{24}Al_4$, $Co_{24}Cr_{24}Fe_{24}Ni_{24}Ho_4$, and $Co_{24}Cr_{24}Fe_{24}Ni_{24}Ti_4$ alloys. Noted first that the $ρ_{twin}$ was defined here as the number of twin boundary intercepts per unit length and second that the for the measurement of $ρ_{twin}$, the 1000 °C (1 h)-annealed alloys were used since they exhibited similar grain sizes (36–42 μm) and $ρ_{twin}$ was found influenced by the grain size.

D value is not achievable, thus we estimated the D value from the average particle area using their average length (1.5 μ m) and thickness (15 nm). The so-calculated values of the Orowan strengthening effects ($\sigma_{\rm Orowan}$) were tabulated in Table 1, showing reasonably good agreement with the experimentally determined values ($\sigma_{\rm Y}-\sigma_{\rm Y,HP}$).

4. Summary and conclusions

To facilitate alloy design based on the CoCrFeNi model alloy through "doping" strategy, in the current paper, we assessed the distinct comonpositional effect of a few representative solute atoms, namely Al, Mo and Ti, on its microstrucrure and mechanical properties. To this end, 4 at.% Al, Mo and Ti were alloyed to the CoCrFeNi alloy to obtain the Co24Cr24Fe24Ni24Al4, Co24Cr24Fe24Ni24Mo4, and Co24Cr24Fe24Ni24Ti4 alloys, respectively. Inconsistency of variables other than alloy solute type was avoided by making the extent of alloying, fabrication method, and the state under which the alloys were tested identical. Based on the current results and analyses, the following conclusions can be drawn:

After room temperature rolling and subsequent 1h-annealing at 800–1100 °C, the single phase nature of the CoCrFeNi alloy was maintained, whereas 800 °C- and 900 °C-annealing led to the respective formation of σ phase and η phase in the 4 at.% Mo- and Ti-doped alloys.

Al and Ti are more effective than Mo in reducing the stacking fault energy (SFE) of the CoCrFeNi alloy, because they can induce more considerable deformation of electronic density, making the gliding of atomic layers easier.

Following identical thermomechnical processing, Al-, Mo-, and Ti-doping causes different extent of solid solution strengthening, grain boundary strengthening as well as secondary phase strengthening. Mo causes the most pronounced solid solution strengthening but does not benefit the grain boundary strengthening, the effectiveness ($k_{\rm HP}$) of which is boosted by the doping Al and Ti. Our thorough analyses suggested first, Labusch instead of Fleischer mechanism is applicable to explain the differences in solid solution strengthening, and second, the observed differences in k_{HP} mainly arise from the different tendency of Al, Mo and Ti to reduce the SFE of CoCrFeNi.

In addition, we determined the value of the dimensionless parameter f in the Labusch model for CoCrFeNi-based alloys and found that this value is applicable to quantitatively predict the solid solution strengthening effects with much broader range of concentration. Also, we observed a close relation between k_{HP} and SFE and found that this relation is likely through the influence of SFE on dislocation cross-slip and hence on the density of generated geometrically necessary dislocation. Although more in-depth studies are needed to provide full and mechanistic understandings, both these findings in fact presents significant values to-

ward designing novel single-phase high-strength CoCrFeNi-based alloys through manipulating the solid solution and grain boundary strengthening by compositional tuning.

Declaration of Competing Interests

None.

Acknowledgements

This work was financially supported by the National Natural Science Foundation of China (No. 51901077), the Science and Technology Innovation Platform and Talent Plan of Hunan Province (No. 2019RS1020), and the open project of State Key Laboratory of Advanced Design and Manufacturing for Vehicle Body (No. 71865003), Hunan University, Changsha, China. YG acknowledges support from NSF DMR 1809640.

References

- [1] Z. Wu, H. Bei, F. Otto, G.M. Pharr, E.P. George, Intermetallics 46 (2014) 131-140.
- [2] A. Gali, E.P. George, Intermetallics 39 (2013) 74-78.
- [3] J.W. Yeh, S.K. Chen, S.J. Lin, J.Y. Gan, T.S. Chin, T.T. Shun, C.H. Tasu, S.Y. Chang, Adv. Eng. Mater. 6 (2004) 299-303.
- [4] B. Cantor, I.T.H. Chang, P. Knight, A.J.B. Vincent, Mater. Sci. Eng. A 375-377 (2004) 213-218.
- [5] T. Yang, S. Xia, S. Liu, C. Wang, S. Liu, Y. Zhang, J. Xue, S. Yan, Y. Wang, Mater. Sci. Eng. A 648 (2015) 15-22.
- [6] Y. Lv, R. Hu, Z. Yao, J. Chen, D. Xu, Y. Liu, X. Fan, Mater. Des. 132 (2017) 392-399
- [7] Y. Lu, X. Gao, L. Jiang, Z. Chen, T. Wang, J. Jie, H. Kang, Y. Zhang, S. Guo, H. Ruan, Y. Zhao, Z. Chao, T. Li, Acta Mater. 124 (2017) 143-150.
- [8] P. Cui, Y. Ma, L. Zhang, M. Zhang, J. Fan, W. Dong, P. Yu, G. Li, R. Liu, Mater. Sci. Eng. A 737 (2018) 198-204.
- [9] T.T. Shun, L.Y. Chang, M.H. Shiu, Mater. Sci. Eng. A 556 (2012) 170-174.
- [10] Y. Tong, D. Chen, B. Han, J. Wang, R. Feng, T. Yang, C. Zhao, Y.L. Zhao, W. Guo, Y. Shimizu, C.T. Liu, P.K. Liaw, K. Inoue, Y. Nagai, A. Hu, J.J. Kai, Acta Mater. 165 (2019) 228-240.
- [11] W.H. Liu, Z.P. Lu, J.Y. He, J.H. Luan, Z.J. Wang, B. Liu, Y. Liu, M.W. Chen, C.T. Liu, Acta Mater. 116 (2016) 332-342.
- [12] G. Qin, R. Chen, H. Zheng, H. Fang, L. Wang, Y. Su, J. Guo, H. Fu, J. Mater. Sci. Technol. 35 (2019) 578-583.
- [13] W.H. Liu, J.Y. He, H.L. Huang, H. Wang, Z.P. Lu, C.T. Liu, Intermetallics 60 (2015)
- [14] S. Vrtnik, S. Guo, S. Sheikh, A. Jelen, P. Koželj, J. Luzar, A. Kocjan, Z. Jagličić, A. Meden, H. Guim, H.J. Kim, J. Dolinšek, Intermetallics 93 (2018) 122–133.
- [15] A. Verma, P. Tarate, A.C. Abhyankar, M.R. Mohape, D.S. Gowtam, Scr. Mater. 161 (2019) 28-31.
- [16] H. Zheng, R. Chen, G. Qin, X. Li, Y. Su, J. Mater. Sci. Technol. 38 (2020) 19–27.
- [17] E. Zhou, D. Qiao, Y. Yang, D. Xu, Y. Lu, J. Wang, J.A. Smith, H. Li, H. Zhao, P.K. Liaw, F. Wang, J. Mater. Sci. Technol. 46 (2020) 201-210.
- [18] Z. Xu, Z. Li, Y. Tong, W. Zhang, Z. Wu, J. Mater. Sci. Technol. 60 (2021) 35-43.
- [19] L.J. Zhang, M.D. Zhang, Z. Zhou, J.T. Fan, P. Cui, P.F. Yu, Q. Jing, M.Z. Ma, P.K. Liaw, Mater. Sci. Eng. A 725 (2018) 437-446.
- [20] W. Huo, H. Zhou, F. Fang, X. Zhou, Z. Xie, J. Jiang, J. Alloys. Compd. 735 (2018) 897-904
- [21] Z. Wu, H. Bei, G.M. Pharr, E.P. George, Acta Mater. 81 (2014) 428-441.
- [22] H. Jiang, K. Han, D. Qiao, Y. Lu, Z. Cao, T. Li, Mater. Chem. Phys. 210 (2018) 43-48.
- [23] G. Kresse, J. Furthmüller, Comput. Mater. Sci. 6 (1996) 15-50.
- [24] J.P. Perdew, K. Burke, M. Ernzerhof, Phys. Rev. Lett. 77 (1996) 3865-3868.
- [25] P.E. Blöchl, Phys. Rev. B 50 (1994) 17953–17979.
- [26] P.J.H. Denteneer, J.M. Soler, Solid State Commun. 78 (1991) 857–861.
- [27] P.J.H. Denteneer, W. van Haeringen, J. Phys. C 20 (1987) L883-L887.
- [28] J.M. Cowley, Phys. Rev. 138 (1965) A1384-A1389.
- [29] J.M. Cowley, Phys. Rev. 77 (1950) 669–675.
- [30] S. Zhao, G.M. Stocks, Y. Zhang, Acta Mater. 134 (2017) 334-345.
- [31] S. Zhao, Y. Osetsky, G.M. Stocks, Y. Zhang, NPJ Comput. Mater. 5 (2019) 13.

- [32] G. Liu, X. Xiao, M. Véron, S. Birosca, Acta Mater. 185 (2020) 493-506.
- [33] F. Long, Y.S. Yoo, C.Y. Jo, S.M. Seo, Y.S. Song, T. Jin, Z.Q. Hu, Mater. Sci. Eng. A 527 (2009) 361–369.
- [34] J.P. Shingledecker, G.M. Pharr, Metall. Mater. Trans. A 43 (2012) 1902-1910.
- [35] F. Chen, Z. Chen, F. Mao, T. Wang, Z. Cao, Mater. Sci. Eng. A 625 (2015) 357-368.
- [36] E.O. Hall, Proc. Phys. Soc. London B 64 (1951) 747-753.
- [37] N.J. Petch, J. Iron. Steel. Inst. 174 (1653) 25-28.
- [38] A.H. Cottrell, Dislocation and Plastic Flow in Crystals, Oxford University Press, Oxford 1953
- [39] J.D. Eshelby, Acta Metall. 3 (1955) 487-490.
- [40] A.W. Cochardt, G. Schoeck, H. Wiedersich, Acta Metall, 3 (1955) 533-537.
- [41] G. Schoeck, A. Seeger, Acta Metall. 7 (1959) 469-477.
- [42] N.F. Mott, F.R.N. Nabarro, Proc. Phys. Soc. 52 (1940) 86–89.
 [43] A.H. Cottrell, B.A. Bilby, Proc. Phys. Soc. A 62 (1949) 49–62.
- [44] L.J. Dijkstra, J. Met. 1 (1949) 252–260.
- [45] R.L. Fleischer, Acta Metall. 9 (1961) 996-1000.
- [46] R.L. Fleischer, Acta Metall. 11 (1963) 203-209.
- [47] J. Friedel, International Series of Monographs on Solid State Physics, Pergamon Press, Oxford. 1964.
- [48] A.J.E. Foreman, M.J. Makin, Philos Mag. 14 (1966) 911-924.
- [49] U.F. Kocks, Philos. Mag. 13 (1966) 541–566.[50] R. Labusch, Phys. Stat. Sol. 41 (1970) 659–669.
- [51] R. Labusch, Acta Metall. 20 (1972) 917-927.
- [52] R. Labusch, J. Appl. Phys. 48 (1977) 4550-4556.
- [53] C.R. Larosa, M. Shih, C. Varvenne, M. Ghazisaeidi, M. Shih, C. Varvenne, Mater. Charact. 151 (2019) 310-317.
- [54] F.G. Coury, M. Kaufman, A. Clarke, Acta Mater. 175 (2019) 66-81.
- [55] I. Basu, J.Th.M.de Hosson, Scr. Mater. 187 (2020) 148-156.
- [56] G.P.M. Leyson, W.A. Curtin, Philos. Mag. 93 (2013) 2428–2444.
- [57] Z. Wu, Y. Gao, H. Bei, Acta Mater. 120 (2016) 108-119.
- [58] I. Toda-Caraballo, Scr. Mater. 127 (2017) 113-117.
- [59] I. Toda-Caraballo, P.E.J. Rivera-Diáz-Del-Castillo, Acta Mater. 85 (2015) 14–23. [60] J. Wang, H. Yang, H. Huang, J. Ruan, S. Ji, J. Alloys. Compd. 798 (2019) 576-586.
- [61] C. Varvenne, W.A. Curtin, Scr. Mater. 138 (2017) 92-95.
- [62] D. Choudhuri, M. Komarasamy, V. Ageh, R.S. Mishra, Mater. Chem. Phys. 217 (2018) 308-314.
- [63] S.G. Ma, S.F. Zhang, J.W. Qiao, Z.H. Wang, M.C. Gao, Z.M. Jiao, H.J. Yang, Y. Zhang, Intermetallics 54 (2014) 104-109.
- [64] J.C. Rao, H.Y. Diao, V. Ocelík, D. Vainchtein, C. Zhang, C. Kuo, Z. Tang, W. Guo, J.D. Poplawsky, Y. Zhou, P.K. Liaw, J.Th.M. de Hosson, Acta Mater 131 (2017) 206-220
- [65] W. Wu, L. Guo, B. Guo, Y. Liu, M. Song, Mater. Sci. Eng. A 759 (2019) 574–582.
- [66] G.E. Dieter, Mechanical metallurgy, McGraw-Hill Higher Education, Mc-Graw-Hill, Berlin, 1986.
- [67] F.J. Humphreys, M. Hatherly, Recrystallization and Related Phenomena, Pergamon Press, Oxford, 2004.
- [68] J. Garstone, R.W.K. Honeycombe, Dislocations and Mechanical Properties of Crystals, Wiley, New York, 1957.
- [69] W. Woo, M. Naeem, J.S. Jeong, C.M. Lee, S. Harjo, T. Kawasaki, H. He, X.L. Wang, Mater. Sci. Eng. A 781 (2020) 139-224.
- [70] H. Parvin, M. Kazeminezhad, Comput. Mater. Sci. 95 (2014) 250-255.
- [71] M. Huang, Z. Li, J. Mech. Phys. Solids 61 (2013) 2454-2472.
- [72] F. He, Z. Wang, B. Han, Q. Wu, D. Chen, J. Li, J. Wang, C.T. Liu, J.J. Kai, J. Alloys. Compd. 769 (2018) 490-502.
- [73] B. Cai, B. Liu, S. Kabra, Y. Wang, K. Yan, P.D. Lee, Y. Liu, Acta Mater 127 (2017)
- [74] P. Yu, Y. Zhuang, J.P. Chou, J. Wei, Y.C. Lo, A. Hu, Sci. Rep. 9 (2019) 10940.
- [75] Y.F. Wen, J. Sun, J. Huang, H. Xing, Chin. J. Nonferrous. Met. 21 (2011) 1664-1667
- S. Guo, C.T. Liu, Prog. Nat. Sci. Mater. Int. 21 (2011) 433-446.
- [77] http://www.webelements.com/.
- [79] O.N. Senkov, D.B. Miracle, Mater. Res. Bull. 36 (2001) 2183-2198.
- [79] S. Mahajan, C.S. Pande, M.A. Imam, B.B. Rath, Acta Mater. 45 (1997) 2633-2638.
- [80] Y.J. Zhang, D. Han, X.W. Li, Scr. Mater. 178 (2020) 269-273.
- [81] Y. Jin, B. Lin, M. Bernacki, G.S. Rohrer, A.D. Rollett, N. Bozzolo, Mater. Sci. Eng. A 597 (2014) 295-303.
- [82] S.V. Astafurov, G.G. Maier, E.V. Melnikov, V.A. Moskvina, M.Y. Panchenko, E.G. Astafurova, Mater. Sci. Eng. A 756 (2019) 365-372.
- [83] S.L. Wang, L.E. Murr, Metallography 13 (1980) 203-224.
- [84] C.Y. Cui, Y.F. Gu, D.H. Ping, H. Harada, T. Fukuda, Mater. Sci. Eng. A 485 (2008) 651-656.
- [85] S.L. Shang, C.L. Zacherl, H.Z. Fang, Y. Wang, Y. Du, Z.K. Liu, J. Phys. Condens. Matter. 24 (2012) 505403.